Bulletin of the JSME Vol.17, No.6, 2023
Journal of Advanced Mechanical Design, Systems, and Manufacturing

Laser beam powder bed fusion of Inconel 718 under high power and scanning speed

Toshi-Taka IKESHOJI*,***, Yusuke TACHIBANA**,****, Makiko YONEHARA*,***
and Hideki KYOGOKU*,***

*Fundamental Technology for Next Generation Research Institute, Kindai University
1 Umenobe, Higashi-Hiroshima, Hiroshima, 739-2116, Japan
E-mail: ikeshoji.tt@hiro.kindai.ac.jp
**Graduate School of Systems Engineering, Kindai University
1 Umenobe, Higashi-Hiroshima, Hiroshima, 739-2116, Japan
***Technology Research Association for Future Additive Manufacturing; TRAFAM
1-10-4, Kaji-Cho, Chiyoda-Ku, Tokyo, 103-0027, Japan
****Nippon Piston Ring Co., Ltd.
1111 Nogi, Nogi-Machi Simotsuga-Gun, Tochigi, 329-0114, Japan

Received: 16 May 2023; Revised: 24 October 2023; Accepted: 24 November 2023

Abstract

The process map area of laser beam powder bed fusion for the nickel-based superalloy Inconel 718 is investigated using high laser power (600-1000 W) and scanning speeds (1500-3500 mm/s). The process map is defined by the surface morphologies (visually inspected) and relative densities of the as-built materials. The effects of the process parameters on the melting and solidification phenomena are observed by high-speed camera imaging, while those on the microstructure of the as-built parts are observed through the scanning electron micrograph (SEM). The process window to build specimens with smooth surfaces and high relative densities was in the laser power range of 700-1000 W and a scanning speed of 1500 mm/s. Notably, the relative density of the specimen built in this process window was slightly lower than that of the specimen built in the current process window of low power (100-400 W) and scanning speed (100-1500 mm/s). High-speed camera observation of the melt pool behavior revealed that the plasma plume was ejected backward in the laser scan direction, and many large spatters were ejected along the plume under the proposed higher power and scan speed conditions. Moreover, the melt pool was unstable, and the laser track displayed an irregular shape. The spatter and unstable melt pool were attributed to the keyhole evolution in the melt pool. The microstructure of the as-built parts presented features similar to those of materials built under the current process window. This research provided process parameters set under high power and scanning speed conditions and enabled the fabrication of dense materials like those produced within the conventional process window. The higher scanning velocity reduces the building time compared to the current process window.

Keywords : Additive manufacturing, Selective laser melting, Fabrication condition, Inconel 718, Microstructure, Melt pool, High-speed imaging

1. Introduction

Recently, additive manufacturing (AM) technology has gained much attention in industrial fields such as aerospace, medical, and automotive. Laser beam powder bed fusion (PBF-LB in ISO/ASTM 5900:2018(ISO/ASTM 52900:2018, 2018), also commonly called LPBF) is one such AM method that has the advantage of manufacturing complex-shaped products in a relatively short time. PBF-LB allows manufacturing of three-dimensional complex-shaped metallic parts that are impossible to manufacture by conventional processes(Gibson et al., 2010). Furthermore,

Paper No.23-00216
[DOI: 10.1299/jamdsm.2023jamdsm0081]

this method can fabricate different alloys, such as stainless steel, titanium and aluminum alloys, and nickel-based superalloys(Yap et al., 2015; Yun et al., 2019). Among nickel-based superalloys, Inconel 718 (IN718), a Ni-Cr-Fe-based ternary alloy, is widely used in the aerospace industry owing to its highly desirable mechanical and chemical properties, such as high yield stress, ultimate tensile stress, and fatigue strengths, low creep, and corrosion and oxidation resistance at both room and elevated temperatures(Donachie and Donachie, 1998; Fu et al., 2009). On the other hand, these properties are undesirable for machining and cold and hot working. Therefore, PBF-LB is applied to manufacture freeform products using IN718 to replace these processing methods.

The total time required to manufacture metal parts by PBF-LB is comparatively shorter than the casting and machining processes. The total time includes feedstock procurement, actual processing, and post-processing. However, the comparative total time advantage of PBF-LB diminishes when the total time includes the time required to design a suitable building plan, i.e., the part orientation in the build chamber and the addition of the support structure. Thus, it is necessary to decrease the actual processing time. One way of achieving this is by increasing the laser scanning speed. However, to our knowledge, the IN718 process parameters in this high scanning speed range have not been publicly reported.

1.1 Process map for the PBF-LB of IN718

The optimal PBF-LB process parameters for IN718 metal powder have been investigated(Scime and Beuth, 2019; Tachibana et al., 2017a; TRAFAM and MAMMS, 2019). The primary PBF-LB parameters are the laser spot size, laser power P, scanning speed v, hatching pitch h, and layer thickness t. Usually, the laser spot size is restricted by the machine laser source, and only the machine user certified by the machine manufacturer can change the laser spot size. The layer thickness determines the z-direction resolution of the built material, and the thinnest layer allowed by the machine is usually selected to minimize the roughness of the sides of the built parts. Thus, the controllable parameters are the laser power, the scanning speed, and the hatching pitch.

Fig. 1 presents a process map summarizing previous works on the laser power and scanning speed for the PBF-LB of IN718 powder using the single-mode continuous wave (CW) laser source. As far as the authors investigated, the current process map is confined to laser power (P) values of P < 400 W and scanning speeds (v) of v < 1500 mm/s. Although some commercially available PBF-LB machines can install the high-power single-mode CW laser sources, the process maps for those machines are not openly available for the range of P > 400 W. In the range of P < 400 W, scanning speed v > 1500 mm/s is too fast to build the dense IN718 material. An area of optimum parameter sets in the process map is called a process window. In addition to a process window framed by a constant laser power in the horizontal direction and constant scanning speed in the vertical direction, diagonal lines with constant energy density values narrow this area. The energy density or volumetric energy density E (J/mm^3) is defined as $E = P/vhz$ where P is the laser power in W, v is the scanning speed in mm/s, h is the hatching pitch in mm, and z is the layer thickness in mm (Bourell et al., 2017). In Fig. 1, the higher and lower boundaries, namely the lines of E = 100 and 25 J/mm^3, respectively, were calculated under an assumption of h = 0.1 mm and t = 0.05 mm. The wider hatching pitch and thicker layer thickness raise the inclination of these lines. Most of the parameter studies confirm the process window, represented as squares (Scime and Beuth, 2019) and triangles (Tachibana et al., 2017a) in Fig. 1. The other parameter sets(Aydinöz et al., 2016; Barros et al., 2019; Bourell et al., 2017; Gao et al., 2019; Ikeshoji et al., 2016; Jia and Gu, 2014; Lesyk et al., 2020; Li et al., 2018; Luo et al., 2019; Ni et al., 2017; Nicoletto, 2019; Sabelkin et al., 2019; X. Wang and Chou, 2019; Witkin et al., 2020), most recommended by machine manufacturers, are represented as circles and fall in the pie-shaped area. In the energy density area along the lines E = 25 and 100 J/mm^3, the relative densities of a specimen are < 99% in some cases. Hence, the process window framed by v < 1500 mm/s, P < 400 W, and E = 25-100 J/mm^3, can be defined solely as “capable to build.”

The area with the desirable feature in a process map changes according to the defining index. The area with a certain quality of the feature is the process window. The process windows in some previously reported parameter studies were determined by visual inspection and the relative densities of the built materials(Scime and Beuth, 2019; Tachibana et al., 2017a) as well as by observation of the cross-section of the laser track shape(Fu et al., 2009). Other researchers have employed the surface roughness and defects observed in the cross-section(Moussaoui et al., 2018), while a more straightforward method was the comparison of the single laser track widths from single-track tests(Sadowski et al., 2016). Nevertheless, a summary of the process maps shows that the area does not differ

[DOI: 10.1299/jamdsm.2023jamdsm0081]

significantly. This agreement suggests that within the pie-shaped area between the lines of E = 40-80 J/mm^3, the PBF-LB process can form IN718 metal powder into the required model shape with relatively high density.

1.2 Mechanical properties

For PBF-LB as-built materials, the static mechanical properties such as the 0.2% proof stress ($\sigma_{0.2}$), the ultimate tensile stress (UTS), and the rapture strain (ε_f) are shown in Fig. 2. These properties form a similar convex curve to energy density. Each of these property indices has a maximum value around E = 80 - 100 J/mm3 and decreased in the lower range and the higher range of the energy density. Internal defects are generated in the lower range of energy density and the higher range to reduce the built relative density of material(Tachibana et al., 2017a). Hence, the lower values of $\sigma_{0.2}$, UTS, and ε_f reflect the increase of the internal defects in the lower and higher energy density ranges. When the energy density value is in the proper range, the built material is almost fully dense without significant internal defects, and the $\sigma_{0.2}$ and UTS are comparable with the wrought, cast, or annealed materials. The ε_f value of PBF-LB-built material is larger than those of wrought and cast material and lower than that of the annealed material. The ε_f of Inconel 718 is affected by the microstructure as well as the internal porosity or the internal defects. The tendency of ε_f values suggests PBF-LB built Inconel 718 has a different microstructure from the wrought, cast, and annealed ones.

The fatigue strength of PBF-LB as-built material is lower than wrought materials(Yamashita et al., 2018). Two significant factors deteriorate the fatigue strength of PBF-LB built material: surface and internal defects. For the as-built material, the near-surface process defects dominate fatigue properties (Nicoletto, 2019; Witkin et al., 2020). The fatigue strength can be enhanced by improving the surface quality. Machining and polishing are straightforward methods for it. However, some complex geometries and the internal hollow shape reject the access of the finishing

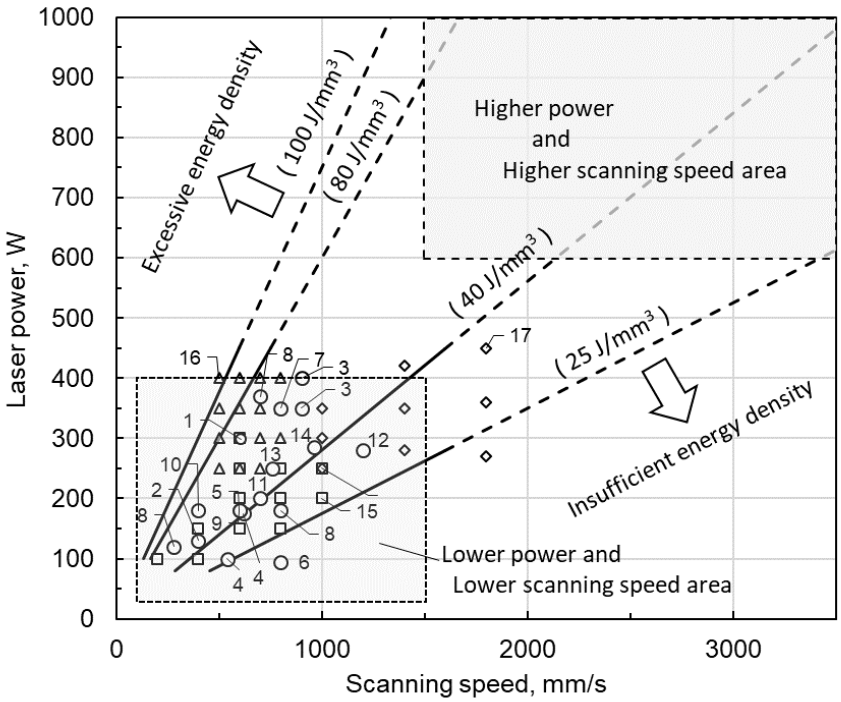

Fig. 1 Process map for the laser beam powder bed fusion of Inconel 718 metal powder. The values of constant energy density lines are calculated for the hatching pitch 0.10 mm, and the powder bed layer thickness 0.05mm. The points are plotted from only the scanning speed and laser power. Some points have different hatching pitch and layer thickness, which means the energy density values are different from the lines drawn in this plot. The numbers inside the graph represent the parameter sets reported by 1) (Ikeshoji et al., 2016), 2) (Jia and Gu, 2014), 3) (Ni et al., 2017), 4) (Aydinöz et al., 2016), 5) (Witkin et al., 2020), 6) (Barros et al., 2019), 7) (Luo et al., 2019), 8) (Sabelkin et al., 2019), 9) (X. Wang and Chou, 2019), 10) (Cheng et al., 2018), 11) (Lesyk et al., 2020), 12) (Gao et al., 2019), 13) (Nicoletto, 2019), 14) (Li et al., 2018), 15) (Scime and Beuth, 2019), 16) Bambi Data Base(Tachibana et al., 2017b; TRAFAM and MAMMS, 2019), and 17) (Moussaoui et al., 2018).

[DOI: 10.1299/jamdsm.2023jamdsm0081]

measures to the as-built surface. The smooth surface must be built for those cases with the proper parameter sets in the process window. The internal defects that lower the fatigue strength can be classified into three types: the irregular-shaped defects generated by the lack of fusion, the large round pores associated with the keyhole formation, and the tiny round gas pores of the residue of powder moisture(Yang et al., 2018). The irregular-shaped defects could be eliminated by increasing the energy density of the PBF-LB process, and the large round pore could be suppressed by increasing the energy density. Hence, when the parameter sets of the PBF-LB process are in the process window, those defects are diminished, and simultaneously, the relative density of the built material increases. Therefore, to improve the fatigue strength of the PBF-LB as-built material, the process windows to minimize the surface roughness and maximize the relative density are required to be provided.

1.3 Metallurgical microstructure of IN718

For the process map, besides the shape-forming indices, the examination of the metallurgical microstructure is necessary. The PBF-LB built material experiences local melting and solidification followed by rapid cooling as well as several bouts of reheating by the nearby laser scanning. Thus, the material might display a different microstructure

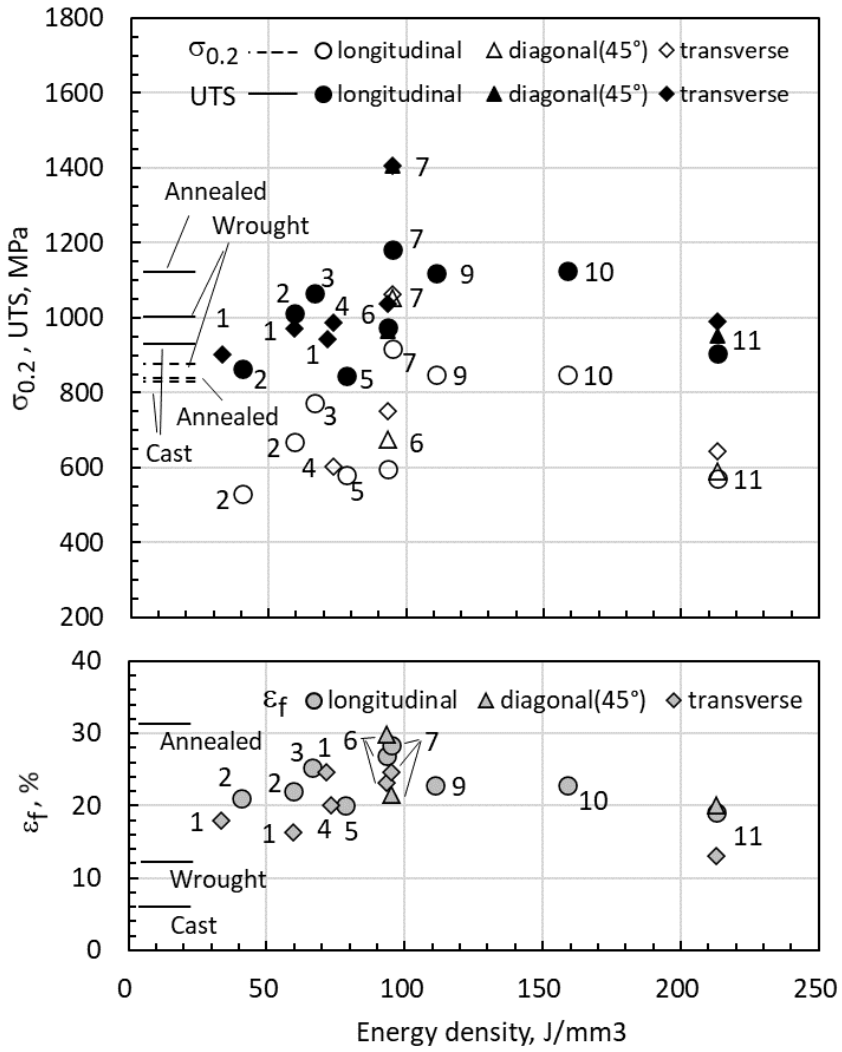

Fig. 2 Mechanical properties and the energy density. PBF-LB as-built Inconel 718 reported by 1) (Tachibana et al., 2017b), 2) (Popovich et al., 2017), 3) (Lu et al., 2015), 4) (Sabelkin et al., 2019), 5) (Aydinöz et al., 2016), 6) Bambi Database (TRAFAM and MAMMS, 2019), 7) (Witkin et al., 2020), 8) (Wang et al., 2016), 9) (Gao et al., 2019), 10) (Zhang et al., 2015), 11) (Chlebus et al., 2015). Wrought and cast Inconel is re ported by A. Sidambe, et al.(Sidambe et al., 2013). Annealed Inconel 718 is taken from MatWeb(MatWeb, 2020a, MatWeb, 2020b, MatWeb, 2020c).

[DOI: 10.1299/jamdsm.2023jamdsm0081]

from other forming methods, such as a fine microstructure, anisotropy, and the precipitate form. Therefore, a process map only defined by the shape-forming indices is insufficient to reveal the characteristics of the PBF-LB built material.

IN718 has a precipitation-hardened microstructure. The γ-Ni phase matrix comprises two precipitate phases, namely a primary γ”-phase (Ni3Nb; D022) and a secondary γ’-phase [Ni3(Al, Ti)]. The material properties of IN718, such as tensile strength, elongation, creep, and fatigue strength, change according to the heat treatment(Hayashi and Kakehi, 2010) and thermal history. Notably, the PBF-LB as-built IN718 material has a complex thermal history revealed by its unique metallurgical microstructure and mechanical properties. The metallurgical microstructure of this material consists of a γ - phase matrix with γ”- and γ’-phase precipitates as well as δ- (Ni_3Nb; orthogonal) and Laves (Ni_2Nb) phase precipitates. These two precipitates adversely affect the mechanical properties of the material(Amato et al., 2012; Chlebus et al., 2015; Zhang et al., 2015). Heat treatment can improve the microstructure and mechanical properties of IN718. The tensile strength increases after solution treatment due to the recrystallization of dendrite microstructures and precipitate formation by the solvation of the Laves phase into the matrix(Zhang et al., 2015). In order to eliminate the void defects caused by insufficient melting or air trapping, hot isostatic pressing (HIP) is sometimes applied to IN718 parts, which strongly influences the tensile stress-strain and cyclic loading behavior of the PBF-LB-built IN718 due to the recrystallization of the matrix(Aydinöz et al., 2016). Thus, thermal treatment and HIP reduce the anisotropic properties arising from the PBF-LB process (Farber et al., 2018).

1.4 In situ observation of the PBF-LB process for IN718

The melting and solidification behavior of the metal powder during the PBF-LB process has been investigated through experiments and numerical simulations to generate the process map and predict the metallurgical microstructure (Araki et al., 2018; Bidare et al., 2018; Khairallah et al., 2016; King et al., 2015; King et al., 2014; Kyogoku and Ikeshoji, 2020; Ly et al., 2017; Matthews et al., 2016). The laser beam irradiates the powder bed and substrate surface during laser scanning to form a melt pool. The melt pool depth (micro-keyhole depth and keyhole formation) is affected by the heat conductance of the subsurface material(King et al., 2014; King et al., 2015). The keyhole is the depression in the melt pool formed by the recoil pressure from metal vapor evaporation. When a keyhole develops in the melt pool, the melt moves dynamically to eject spatters and shake the melt pool tail, making it unstable. This dynamical melt flow generates gas pore defects, lack-of-fusion defects, and denudation zones(Khairallah et al., 2016). By plume emission, denudation forms a cleaned powder bed zone along the laser track (Matthews et al., 2016). The plume, which comprises a mixture of the metal vapor jet and plasma emitted from the melt pool, creates an ambient gas flow in which the detached melt and metal powder ride(Bidare et al., 2018). The plume dynamics and denudation have been observed by high-speed imaging, and their nature has been analyzed by numerical simulation(Ly et al., 2017). High-speed and thermal distribution images have confirmed these melting and solidification phenomena (Araki et al., 2018; Kyogoku and Ikeshoji, 2020). The laser ablation melts the metal powders and their substrate, simultaneously rapidly evaporating them to emit the plasma plume. The recoil momentum caused by metal evaporation exerts pressure on the melt pool surface and forms a cavity, the so-called keyhole. Because the plume velocity is significantly high, the plume occasionally blows out the molten metal as spatters, and the plume flow denudes the powder near the laser track. Thus, observing these phenomena is necessary to reduce defects and obtain the process map.

1.5 Aims of the research

The process maps of the PBF-LB of IN718 are currently confined to relatively low power and scanning speed areas, mainly due to the laser source on the commercially available PBF-LB machines. From an energy density viewpoint, the bounding lines of the constant energy density values become broader in the higher scanning speed area in the process map. Thus, if a higher laser power source is available, the higher power and scanning speed area might provide a wider variety of parameter set combinations. To build higher quality parts, several different parameter sets are used in one layer according to the laser paths of the up-skin, the down-skin, the core, the contour of the parts, and the support structure(Krishnan et al., 2014; Townsend et al., 2016; Witkin et al., 2020). The wider variations may provide options to find suitable parameter sets for those laser paths. However, A high scanning speed significantly increases the laser track's cooling rate. In the solidified area, this increased rate possibly changes the metallurgical

[DOI: 10.1299/jamdsm.2023jamdsm0081]

microstructure, i.e., precipitation of the δ- and Laves phases. A higher laser power and scanning speed may also change the melt pool, spatter behavior, and plume.

With these facts in mind, in this research, we investigated the process map for the PBF-LB process of IN718 in high laser power (600-1000 W) and scanning speed area (1500-3500 mm/s) using a custom-made PBF-LB machine with a 1 kW fiber laser source. The surface morphology and relative density defined the process map. The metallurgical microstructure was also investigated by studying the cross-sections of the as-built materials. Finally, the melting and solidification phenomena during the PBF-LB process under these conditions were observed by high-speed camera imaging.

2. Prediction of process map for high power and high scanning speed

In the laser powder bed fusion (PBF-LB) process, a laser scans over a thin powder layer covering the bulk material. The process can be modeled as a point heat source moving over a semi-infinite body. Under this framework, an approximate process map of PBF-LB can be constructed using the dimensions of the melt pool. Our approach adapts Christiansen's N-D diagram technique(Christiansen et al., 1965), initially developed in arc welding and based on Rosenthal's solution for a moving point heat source(Rosenthal, 1946).

This method has been further refined since melt pools are unstable under fast scanning velocity conditions. Modifying Christiansen's N-D diagram technique including the melt pool dimensions of the powder bed bottom, can determine laser power, scanning speed, and hatching pitch. In addition, we incorporate the Rayleigh instability prediction of Rombouts et al. (Rombouts et al., 2006) to predict the occurrence of the Balling phenomenon.

2.1 Estimation of melt pool dimensions

Rosenthal's solution for a moving point heat source over a semi-infinite body is expressed as follows (Grong, 1997).

$$T - T_0 = \frac{kP}{2\pi\lambda} \cdot \frac{1}{R} \cdot exp\left[-\frac{v}{2\alpha}(R + x)\right] \tag{1}$$

P and v are the laser pressure and the scanning velocity. k is the laser absorption rate to the powder bed. R the radius T is the temperature, and T_0 is the build plate temperature. λ is the thermal conductivity, and α is the thermal diffusivity; $\alpha = \lambda/\rho c_p$ where ρ and c_p are the density and the heat capacity, respectively.

When the above formula is non-dimensionalized using $2\alpha/v$ and $T_m - T_0$ as a reference length and a reference temperature using the melting point T_m,

$$\xi = \frac{x}{2\alpha/v} = \frac{vx}{2\alpha}\ ,\ \psi = \frac{vy}{2\alpha}\ ,\ \zeta = \frac{vz}{2\alpha}\ ,\ \varrho = \frac{vR}{2\alpha} = \sqrt{\xi^2 + \psi^2 + \zeta^2}\ ,\ \Theta = \frac{T - T_0}{T_m - T_0} \tag{2}$$

Non-dimensional Rosenthal's solution can be expressed as follows (Fig. 3),

$$\frac{\Theta}{N} = \frac{1}{\varrho} exp(-\varrho - \xi) \tag{3}$$

N is Christiansen's operating parameter,

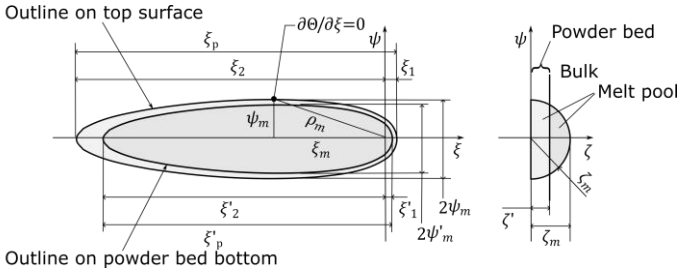

Fig. 3 Schematics of melt pool dimensions

[DOI: 10.1299/jamdsm.2023jamdsm0081]

$$N = \frac{kPv}{4\pi\alpha\lambda(T_m - T_0)} \quad or \quad \frac{kPv}{4\pi\alpha^2\rho c_p(T_m - T_0)} \tag{4}$$

The melt pool width w can be obtained by considering $\partial\Theta/\partial\xi = 0$ for the peripheral of the melt pool on the top surface, i.e., a contour line of $\Theta = 1$. At the point $(\xi_m, \psi_m, 0)$ and the radius ϱ_m where the condition is satisfied,

$$\xi_m = -\frac{{\varrho_m}^2}{1+\varrho_m} \tag{5}$$

The half-width of the melt pool and the depth are

$$\psi_m = \zeta_m = \sqrt{\varrho_m^2 - \xi_m^2} = \frac{\varrho_m}{1+\varrho_m}\sqrt{1+2\varrho_m} \tag{6}$$

Substitution of Eq. (5) into the non-dimensional Rosenthal's solution Eq.(3) gives

$$N = \varrho_m \, exp\left(\frac{\varrho_m}{1+\varrho_m}\right) \tag{7}$$

In practice, the first step in determining the melt pool width is calculating N. Subsequently, the non-linear equation mentioned above is solved to obtain the value of ϱ_m. Then, the melt pool width w and depth d are

$$w = 2\psi_m \cdot 2\alpha/v \tag{8}$$
$$d = w/2 \tag{9}$$

The melt pool length L is calculated from the non-dimensional melt pool length ξ_p . When the leading point of the melt pool is $(\xi_1, 0, 0)$ and the trailing point $(-\xi_2, 0, 0)$,

$$\xi_1 \, exp \, 2\xi_1 = N, \quad \xi_2 = N \tag{10}$$
$$\xi_p = \xi_1 + \xi_2 \tag{11}$$

Then

$$L = \xi_p \cdot 2\alpha/v \tag{12}$$

2.2 Melt pool dimensions on the powder bed bottom.

When the powder bed thickness is z or $\zeta' = vz/2\alpha$ in non-dimensional form, the width of the melt pool on the powder bed bottom is

$${\psi_m}' = \sqrt{\psi_m^2 - \zeta'^2} \tag{13}$$

because a cross-section of the melt pool is a semicircle for Rosenthal's solution. Then,

$$w' = \sqrt{w^2 - 4z^2}/2 \quad or \quad \sqrt{d^2 - z^2} \tag{14}$$

On the powder bed bottom, substitution of head tip of melt pool $(\xi_1', 0, \zeta')$ in the non-dimensional Rosenthal's solution gives the bow length of the melt pool ξ_1'. Similarly, the tail length of the melt pool on the powder bed bottom ξ_2' can be obtained by the substitution of $(\xi_2', 0, \zeta')$. Then, the melt pool length on the powder bottom is

$${\xi'}_p = {\xi'}_1 + {\xi'}_2 \tag{15}$$
$$L' = {\xi'}_p \cdot 2\alpha/v \tag{16}$$

2.3 Rombout's Rayleigh instability analysis

The occurrence of balling phenomena offers a potential explanation for the correlation between parameter sets and the oscillation observed in the melt pool tail while forming a single laser track on a powder bed. Rombouts et al.

[DOI: 10.1299/jamdsm.2023jamdsm0081]

(Rombouts et al., 2006) elucidated the balling phenomenon, ascribing the swinging motion of the melt pool tail to Rayleigh's instability (Rayleigh, 1892). The duration required for the cylindrical flow to disintegrate can be referred to as the break-up time t_b.

$$t_b = 2.913\sqrt{\frac{\rho(w/2)^3}{\gamma_{LV}}} \tag{17}$$

where, γ_{LV} is the surface tension of the melt, ρ is the density, and w is the width of the melt pool or the laser track.

In the case of the PBF-LB process, the melt pool undergoes solidification within a defined period, referred to as t_s. When $t_b < t_s$, the melt pool experiences a fragmentation of its tail. If a detached portion of molten material possesses a sufficient volume, it agglomerates and forms a molten ball, i.e., the balling phenomenon. The length of the melt pool at the onset of instability can be represented as vt_b. Comparing the length of the melt pool at the onset of instability vt_b, with the melt pool length L estimated using Christiansen's N-D diagram technique, the condition for the occurrence of melt pool instability can be expressed as:

$$vt_b < L \tag{18}$$

2.4 Prediction of the process parameters set

Using Christiansen's N-D diagram technique, the dimensions of the melt pool during laser scanning on IN718 were estimated using the PBF-LB parameter set outlined in Table 1. The relevant material properties of Inconel 718 can be found in Table 2. The obtained results are presented in Fig. 4, revealing that the melt pool width (w) ranged from 100 to 200 µm, the length (L) ranged from 1900 to 3250 µm, and the depth varied between 50 and 100 µm. Furthermore, on the powder bed bottom, the melt pool width (w') was estimated to be between 40 and 175 µm, while the length (L') fell within the range of 500 to 3000 µm. On the other hand, Rombout's Rayleigh instability analysis was conducted using to determine the break-up length for the melt pool to become unstable, and the corresponding results are depicted in Fig. 5. The calculated break-up length (vt_b) required for forming the melt ball ranged from 200 to 360 µm. This value of vt_b is much shorter than the melt pool length on the top surface L. Therefore, the melt pool is unstable and broken up, and the balling phenomena will occur for the whole range in this analysis.

The analysis of the melt pool width concerning the hatching pitch reveals distinct regions indicating various characteristics of the built material. These regions can be described as follows (Fig. 6):

Region	Condition	Material	Surface
I	$h < w'$	Full density	Depends on melt pool stability
II	$w' < h < w$	Lack of fusion defects	Depends on melt pool stability
III	$w < h$	Open grooves or ditch, and open pores	Uneven
IV	$w/2 = d < h$	Fail to build	-

The optimal process window is found in region I when considering the built material density and internal defects. In this region, the relative density of the material remains close to 100%, as LOF defects are minimized. Regions I and II also offer effective control over surface roughness, ensuring the absence of open grooves and pores. However,

Table 1 PBF-LB parameters set

Parameter	Units	Value
Laser spot diameter, 2ω	µm	100.
Laser power, P	W	600-1000
Scanning speed, v	mm/s	1500-3500
Hatch pitch, h	mm	0.150
Layer thickness, z	mm	0.050
Base plate temperature, T_0	ºC	50.

Table 2 Physical properties of IN718

Property	Units	Value
Density, ρ	kg/m^3	8190.[1]
Laser absorption rate, k	--	0.3[2]
Specific heat capacity, c_p	J/(kg K)	435. [1]
Surface tension coefficient, γ_{LV}	N/m	1.823[3]
Thermal conductivity, λ	W/(m K)	11.4[1]
Thermal diffusivity, $\alpha = \lambda/\rho c_p$	m^2/s	3.20×10^{-6}
Liquidus point, T_m	ºC	1336. [1]

1: Matweb (MatWeb, 2020b) 2:Ikeshoji et al. (Ikeshoji et al., 2016). 3: Brooks et al.(Brooks et al., 1996)

[DOI: 10.1299/jamdsm.2023jamdsm0081]

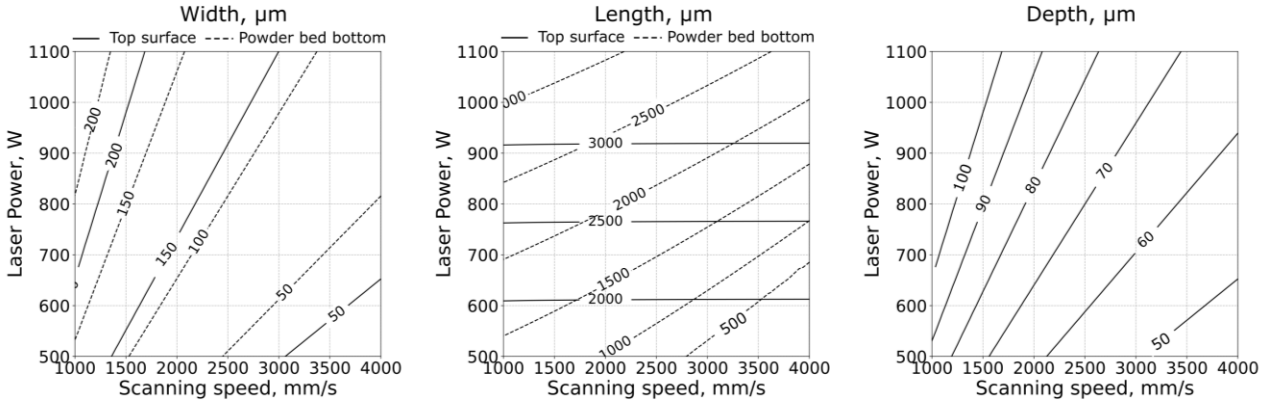

(a) (b) (c)

Fig. 4 Melt pool dimensions estimated using Christiansen's N-D diagram technique based on Rosenthal's solution; (a) width, (b) length, and (c) depth.

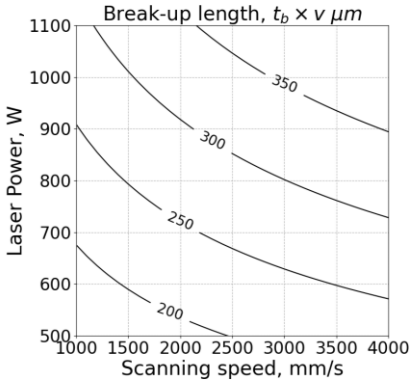

Fig. 5 Rombout's Rayleigh instability analysis for the balling phenomena; break-up length to form the melt ball

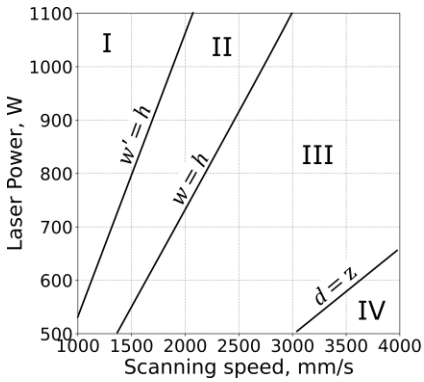

Fig. 6 Process map of PBF-LB/IN718 for high laser power and high scanning speed area predicted using the melt pool dimensions.

it is essential to be cautious of potential issues arising from unstable melt pool oscillation during the process, which can result in a roughened solidified surface. This instability may also lead to the emission of spatters, which can further contribute to surface roughness. Region III represents a distinct phase where open grooves align to form girder-like structures. Consequently, surface characteristics parameters that are sensitive to peaks and valleys, such as maximum surface height (Sz), maximum peak height (Sp), and maximum pit depth (Sv), exhibit larger values within this region.

However, the instability analysis of the melt pool length consistently indicates the presence of balling phenomena, upon the current analysis within the range of P =500-1000 W and v = 1000-4000 mm/s. Eventually, the predictions made by Rombout's Rayleigh instability analysis contradict those of Christiansen's N-D diagram technique. Consequently, experimental verification becomes imperative to examine the density of the built material's surface morphology and the stability of the melt pool.

3. Material and methods

3.1 Experimental apparatus

The Technology Research Association for Future Additive Manufacturing (TRAFAM) testbed machine for PBF-LB was employed to build specimens, define the process map, and monitor the melting and solidification phenomena

[DOI: 10.1299/jamdsm.2023jamdsm0081]

(Fig. 7(a)). The TRAFAM testbed machine was equipped with a 1 kW single-mode CW fiber laser source with a wavelength of ~1070 µm. The laser spot size d_{90} could vary in the range ø90-ø600 µm. The laser spot size d_{90} was defined as the circle's diameter through which 90% laser power passes, and the machine manufacturer specified it. The recoater used the drop-down method to form the powder layer, in which the metal powder was fed by dropping from the powder tank, which was not the method using the dosing table or the powder feed reservoir. The minimum layer thickness was 30 µm. The building table (250 × 250 mm) was covered with a building plate (250 × 250 mm) for regular use. The building table contained regularly spaced screw holes to which several smaller base plates could be fixed. This experiment used a 127 × 127 × 20 mm stainless steel base plate. The building chamber was filled with inert gas (argon or nitrogen) and circulated to maintain a low oxygen content.

A high-speed camera was installed inside the building chamber of the TRAFAM testbed machine for high-speed imaging (Fig. 7(b)). The machine had a closed space next to the building chamber. After removing the sidewall from the space, a high-speed camera was placed there, and its long lens barrel stuck out to the building chamber. The light source was placed outside the machine, and its guide cable was inserted into the building chamber through a hermetically sealed hole. The lighting spotted a building surface from the opposite side of the high-speed camera.

3.2 Specimen preparation

Gas-atomized IN718 powder (Sanyo Special Steel Co., Ltd.) was prepared in this research. The chemical composition in its mill test report is listed in Table 3. The mean particle diameter of the IN718 powder was ~ϕ30 µm, and the scanning electron micrograph indicated that most of the particles were spherical (Fig. 8).

To obtain a process map between the laser power and scanning speed, we built cuboid specimens with dimensions 16.0 × 12.2 × height 15.0 mm with a 2.0 mm height support structure between the base plate and the bottom of the cuboids.

The building conditions included a hatching pitch of 0.15 mm and a layer thickness of 0.05 mm. The laser power and scanning speed were varied to weave a matrix: (600, 700, 800, 900, 1000 W) × (1500, 2000, 2500, 3000, 3500 mm/s) (Table 4). Apart from the conditions in this matrix, values of 900 and 1000 W and 4000 mm/s were also conducted for the relative density measurements and observation of the laser scanning process. With a scanning speed of 4000 mm/s, these conditions were introduced to obtain results for the maximum scanning speed that can be operated with the galvanometer mirror of this PBF-LB machine. The laser spot diameter was set to d_{90} = ø100 µm ($d_{86.5}$ = ø93 µm). The laser scanning strategy was raster scanning without strips and domains. The scanning direction

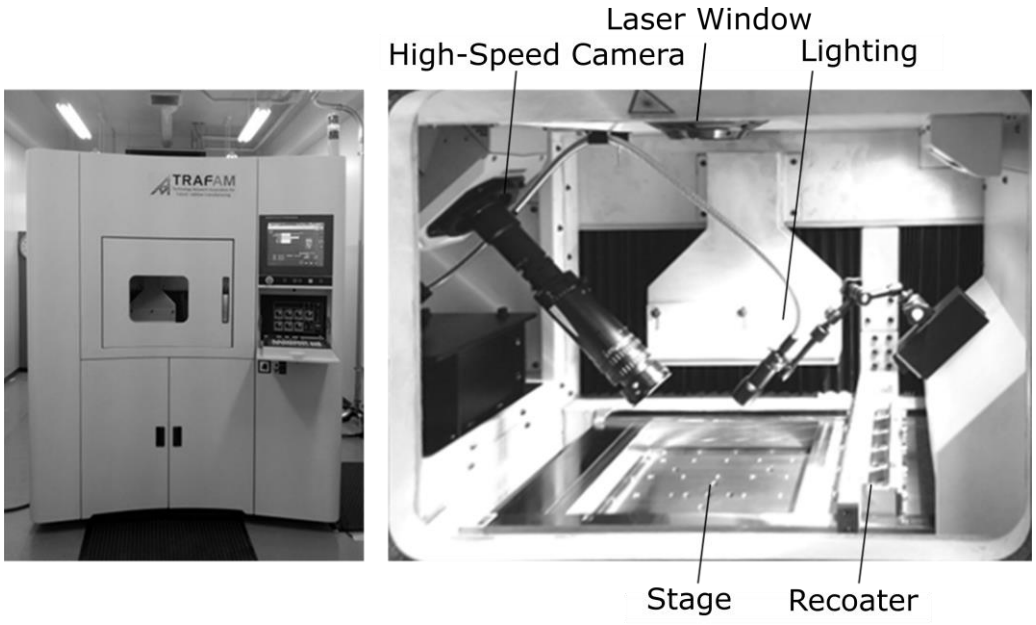

(a) (b)

Fig. 7 TRAFAM testbed for laser beam powder bed fusion. (a) Appearance and (b) interior of its building chamber, including the high-speed camera.

[DOI: 10.1299/jamdsm.2023jamdsm0081]

was rotated 90º layer by layer. A raster scanning direction was parallel to the side of the base plate. The perimeter scanning was not conducted.

Fig. 9 illustrates the appearance of the built cuboid specimens. A 16.0 mm length side of each cuboid made an angle of 30º with a side of the base plate. Cuboids were separated from the base plate using a grinding wheel while supplying a water-soluble cutting fluid.

3.3 Generation of the process map

The process map for the proposed higher speed and laser power ranges was evaluated by visual inspection and roughness index measurement of the surface morphology and the measured relative densities of the built samples.

The surface morphology of each cuboid specimen was observed using a JEOL JSW-7800F scanning electron microscope (SEM). The surface morphology was categorized into three types using the following criteria:

(a) Smooth surface: continuous smooth tracks adjacent to each other without a ditch.
(b) Rough surface: continuous tracks of uneven width adjacent to each other without a ditch.
(c) Discontinuous surface: ditch between tracks, some with uneven width.

For the top horizontal surface of each cuboid, the surface roughness indices were measured with a Zygo NewView 8000/9000 optical surface profiler, which can measure the 3D surface morphology and calculate various surface

Table 3 Chemical composition of the Inconel 718 powder, in mass%, balance Fe.

Element	Ni	Cr	Fe	Nb	Mo	Ti	Al	Mn	Si
Mass%	52.36	19	Bal.	5.16	3.07	0.99	0.47	0.17	0.16

N	Cu	Co	O	C	P	S	B
0.077	0.03	<0.010	0.02	0.004	0.003	0.002	<0.001

Table 4 Matrix of the scanning speed, laser power, and energy density.

		Scanning speed, mm/s				
		1500	2000	2500	3000	3500
Laser power, W	1000	88.9	66.7	53.3	44.4	38.1
	900	80.0	60.0	48.0	40.0	34.3
	800	71.1	53.3	42.7	35.6	30.5
	700	62.2	46.7	37.3	31.1	26.7
	600	53.3	40.0	32.0	26.7	22.9

Energy density, J/mm^3

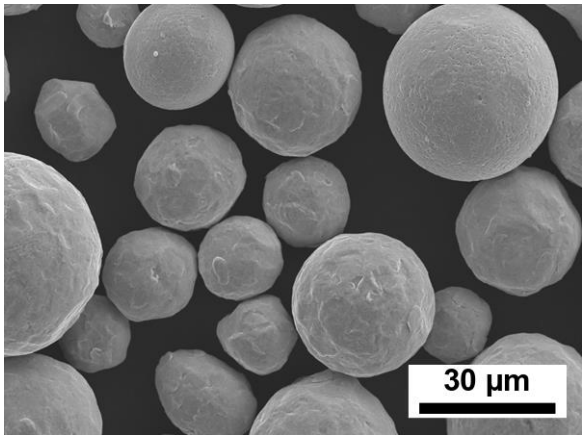

Fig. 8 Scanning electron micrograph of the Inconel 718 powder.

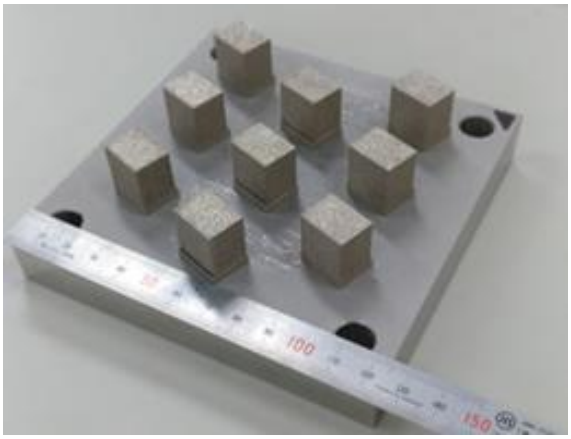

Fig. 9 Photograph of the as-built cuboid Inconel 718 specimens.

[DOI: 10.1299/jamdsm.2023jamdsm0081]

roughness indices. In this research, the arithmetical mean height of the surface (Sa), root-mean-square deviation of the surface (Sq), skewness (Ssk) and kurtosis (Sku) of the 3D surface texture height distribution, maximum surface height (Sz), maximum peak height (Sp), and maximum pit depth (Sv) were obtained.

The densities of the as-built specimens were measured by the Archimedes method, and relative densities were calculated using a reference density value of 8.19 g/cm^3. The criteria to categorize the relative density values were as follows:

(a) optimum: >99%
(b) moderate: 97%< and <99%
(c) low: <97%

These criteria were based on the relationship between the relative density and the distribution of defects inside the PBF-LB-built Inconel 718 material(Tachibana et al., 2017b). The built material with a relative density >99% had no optically observable defects, although the micro-gas pore defects existed inside. On the contrary, the built material with <97% included many large defects generated by the lack of fusion.

3.4 Observation of the microstructure

The cuboid cross-sections were observed macroscopically using an optical microscope (OM). Using a low-speed cutting machine equipped with a diamond wheel while supplying the cutting coolant, a cuboid was cut perpendicular to the side with a length of 16.0 mm. In this way, a vertical cross-section of 16.0 × 15.0 mm was obtained.

The vertical cross-section of each cuboid was polished using abrasive papers at first and mirror-finished using the polishing slurry with 0.1μm alumina powder. For this surface, electrolytic etching was conducted in 10% oxalic acid with a 6 V DC supply for the etching time of ~30s(ASTM A763-15, 2015; Bramfitt and Benscoter, 2001; JIS G 0571:2003, 2003).

The microstructure was observed using a JEOL JSW-7800F SEM. The cross-section surface was etched for a shorter etching time than the OM specimen. Additionally, the element distribution was observed by energy-dispersive X-ray spectroscopy (EDS).

3.5 Observation of the laser scanning process

For the observation of the laser track and melt pool, a high-speed camera (Photron FASTCAM SA-Z) with a zoom lens system (Zeiss APO-16) was installed inside the building chamber (Fig. 7 (b)). The high-speed camera could record a 1 × 5 mm area at a frame rate of 50,000 fps. The light of the 20 W fluorescent lamp was delivered by optical fiber to the powder bed surface.

4. Results and discussion

4.1 Surface morphology

Fig. 10 summarizes the surface morphology observed through SEM. For a scanning speed of 1500 mm/s and laser power in the 700-1000 W range, the surface was relatively smooth, and the laser track was straight. The laser tracks were uneven with small ditches or elongated open pores between them for the same scanning speed (1500 mm/s) but a lower laser power (600 W). At a higher scanning speed (v>2000 mm/s, P=600-1000 W), the surface was uneven, and many large spatters were stuck to it. The spatter diameter was 50-100 μm. Most of these surfaces comprised relatively large open pores. The size of open pores was 50-200 μm. Surfaces with scan speeds v >2500 mm/s and laser powers P<700 W displayed crosshatch or basket-like patterns. In this case, because of the insufficient energy density, the laser track was too narrow to be joined, and the scanning directions for each layer were perpendicular to each other, forming a crosshatch pattern.

Fig. 11 illustrates the relationship between the surface roughness indices and energy density values. The Sa value decreased with increasing energy density, revealing that the surface became smoother at higher energy densities. The

Sku values, which describe the sharpness of the roughness profile, were 3 ± 1; i.e., the height distribution on each surface was normal and almost in Gaussian form. The Ssk values of almost zero compared with Sa values indicated that the normal distribution was symmetrical. Thus, the Sq values could be compared, revealing that these values decreased with increasing energy density. According to the Sa, Sq values, with an increase in energy density, the surface became smoother without any significant deviation from the average plane of the surface. This tendency

[DOI: 10.1299/jamdsm.2023jamdsm0081]

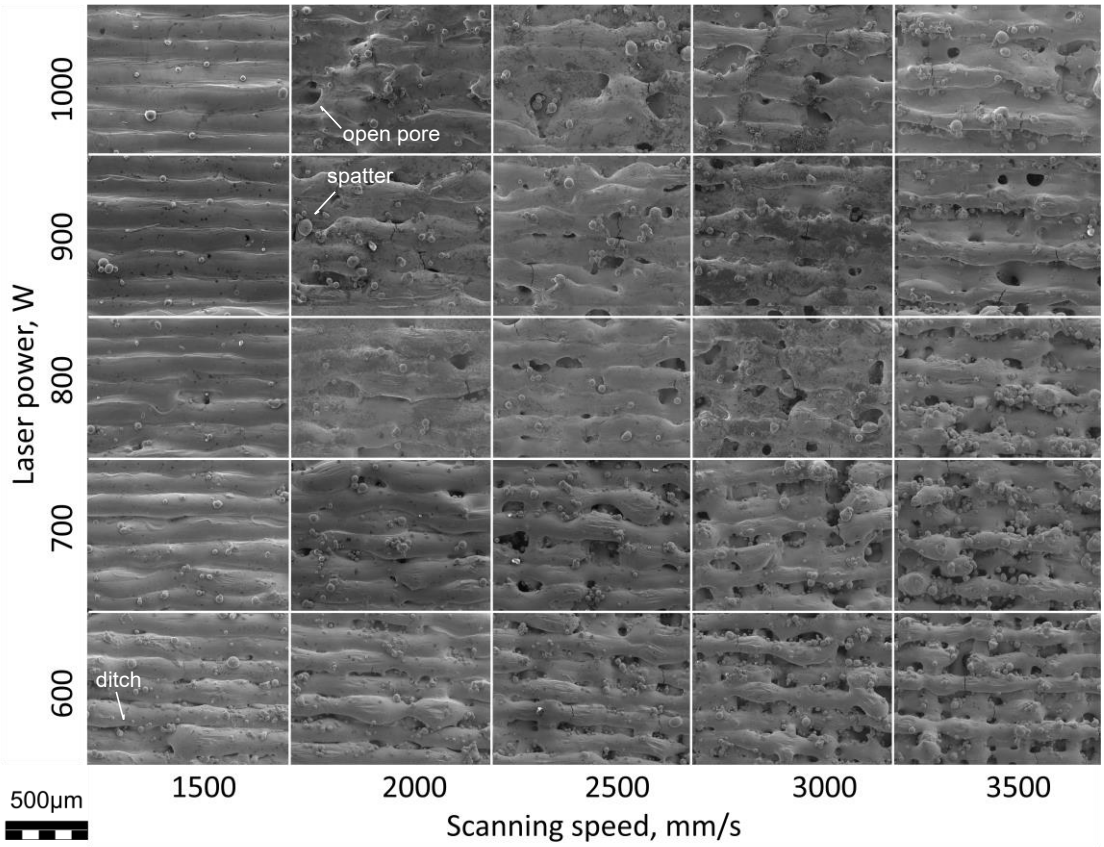

Fig. 10 Secondary electron images of the surface morphology of the PBF-LB-built Inconel 718 specimens.

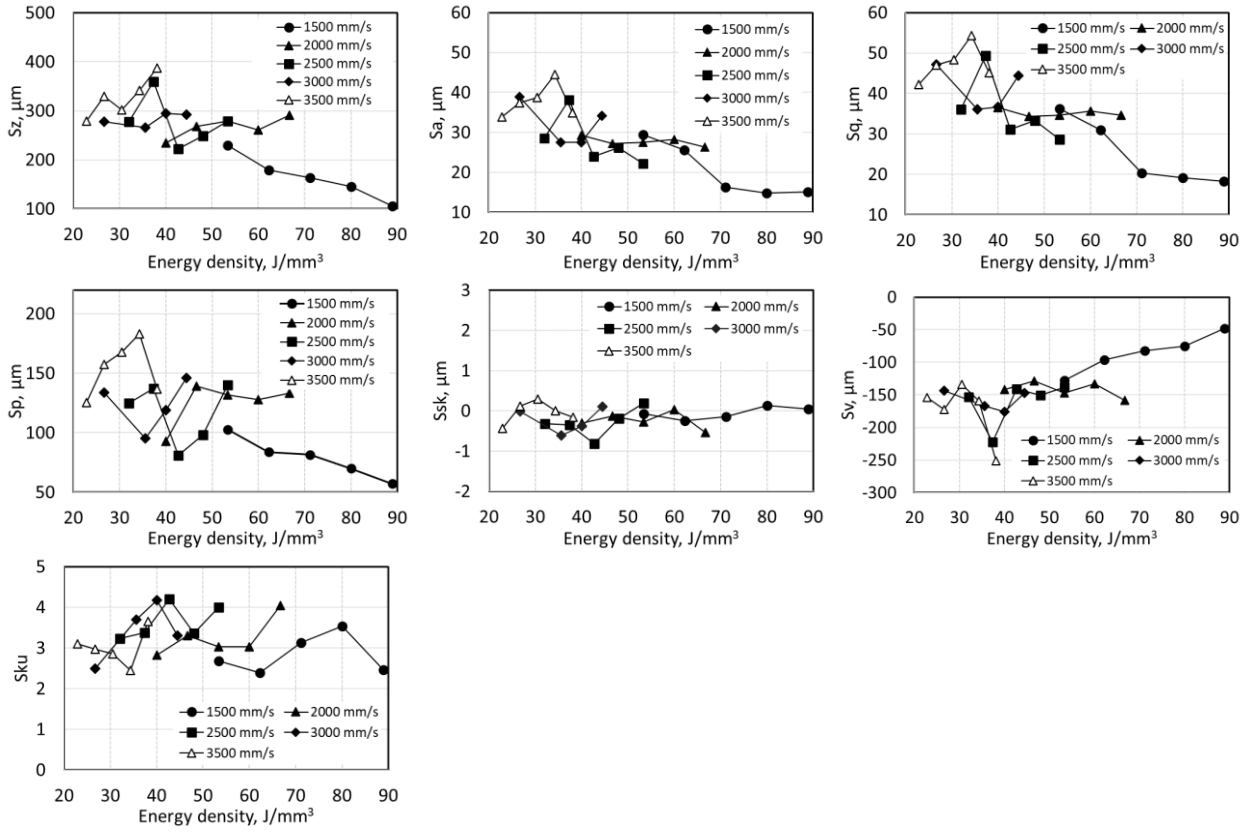

Fig. 11 Surface roughness indices of the PBF-LB-built Inconel 718 specimens.

[DOI: 10.1299/jamdsm.2023jamdsm0081]

coincides with the results reported by Moussaoui et al. in the lower laser power and scanning speed area (X. Wang and Chou, 2019). However, our Sa values are slightly higher than their results.

The parameter Sz is defined as Sp + Sv. A large Sp value indicates that spatters, separated tracks, and balls adhere to the top surface. Conversely, a large Sv value represents deep grooves and open pores on the surface. Specimens with scan speeds >2000 mm/s displayed Sp values between 100 and 200 μm. Moreover, the Sz, Sp, and Sv values decreased at higher energy densities, which indicates that the surface became smooth without large spatters or deep pits at high energy densities.

Fig. 12 depicts a process map defined by the surface morphology. In the figure, the categories of (a) smooth, (b) rough, and (c) discontinuous surfaces are represented as circles, triangles, and crosses, respectively. The specimens in category (b) were built with higher energy densities >35 J/mm^3, which were the values predicted to be sufficient to build a dense material. However, according to the surface morphology, they were expected to contain internal defects. The process map defined by the surface morphology agreed with the process map predicted using the modification of Christiansen's N-D diagram technique, including melt pool dimensions on the powder bed bottom (Fig. 6).

4.2 Effect of the energy density on the relative density and microstructure

The secondary electron images of the cross-section revealed the internal defects of the as-built specimens (Fig. 13(a)-(d)). A few pores appeared in specimen (a), with an energy density of 62.2 J/mm3, and the relative density was >99.2 %. At an energy density of 53.3 J/mm^3 (b), a few round pores were generated, while at the lower energy densities of 48.0 J/mm^3 (c) and 26.7 J/mm^3 (d), a high number of lack-of-fusion defects were observed.

Fig. 13 (e) illustrates the relationship between the relative density and energy density. The plot includes the data for the lower scanning speed (500-1000 mm/s) and laser power (200-1000 W) specimens(Tachibana et al., 2017b). The data revealed that the relative density increased drastically with increasing energy density; however, a 99% relative density was only obtained for the specimens built with a scanning speed of 1500 mm/s. Although the energy densities for some specimens built with 2000 and 2500 mm/s (>50 J/mm^3) matched those observed for the 1500 mm/s specimens, their relative densities were <97%. Therefore, we assumed that the scanning speed might be one of the primary factors affecting the relative density in the high scanning speed and laser power area.

The process map defined by relative densities (Fig. 14) shows that cases with relative densities >99% are

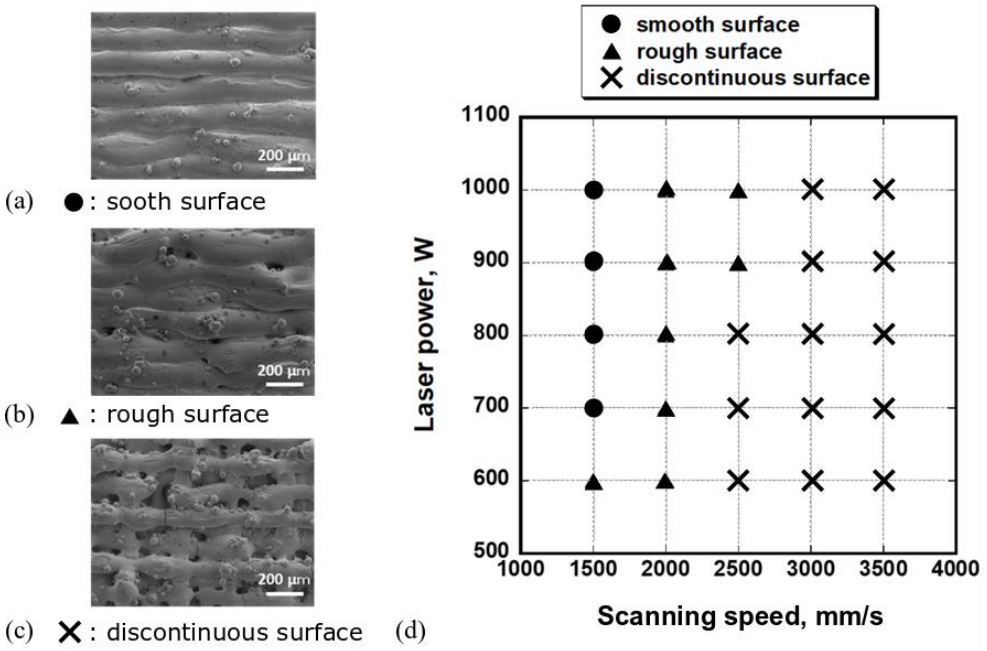

Fig. 12 Process map in terms of the scanning speed and laser power evaluated by the surface morphology and surface roughness results.

[DOI: 10.1299/jamdsm.2023jamdsm0081]

concentrated in the scanning speed range of 1500 mm/s, with no visible effect observed from variations in laser power between 600-1000 W. Conversely, low relative density cases are predominantly observed at scanning speeds exceeding 2500 mm/s. The relative density-based process map exhibits significant similarities to the process map evaluated by surface morphology, suggesting a potential relationship between relative density and surface characteristics. The PBF-LB process involves the compilation of melt layers and can be influenced by the surface morphology of the previous layer, thereby impacting defect formation. For example, spreading a powder bed on a rough surface can alter the melt pool depth and stability, leading to lack-of-fusion defects. Furthermore, large spatters on the solidified surface can impede proper powder filling in subsequent steps, resulting in the formation of voids that contribute to lack-of-fusion defects.

The process map defined by relative density closely corresponds to the process map predicted using a modification of Christiansen's N-D diagram technique with the inclusion of melt pool dimensions on the powder bed

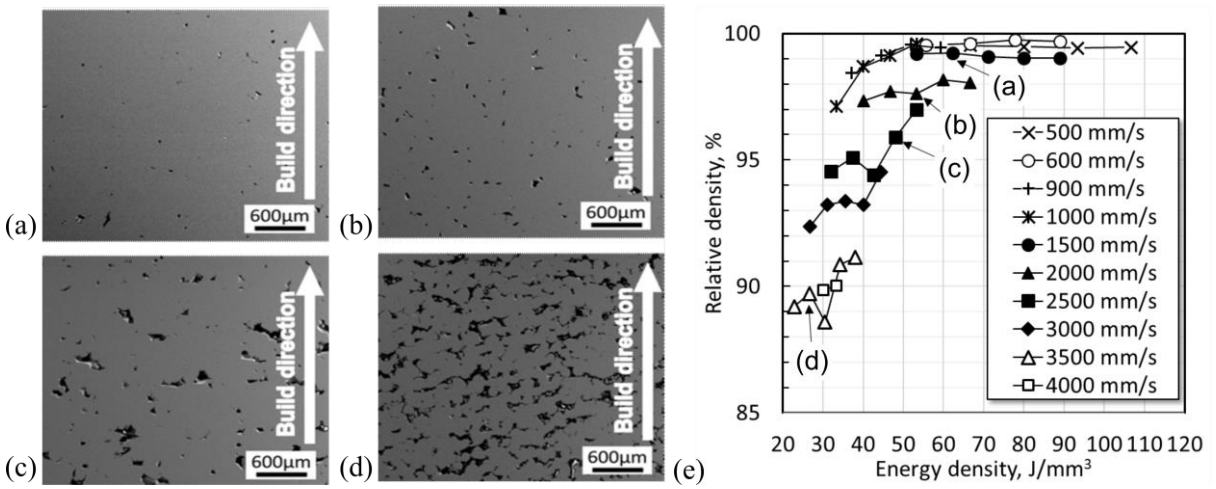

Fig. 13 Relationship between the relative density and energy densities and corresponding micrographs of the as-built specimens at respective scanning speeds, laser powers, and energy densities of (a) 1500 mm/s, 700 W, and 62.2 J/mm3; (b) 2000 mm/s, 800 W, and 53.3 J/mm3; (c) 2500 mm/s, 900 W, and 48.0 J/mm3; and (d) 3500 mm/s, 700 W, and 26.7 J/mm3, (e) plot of the relative density versus the energy density.

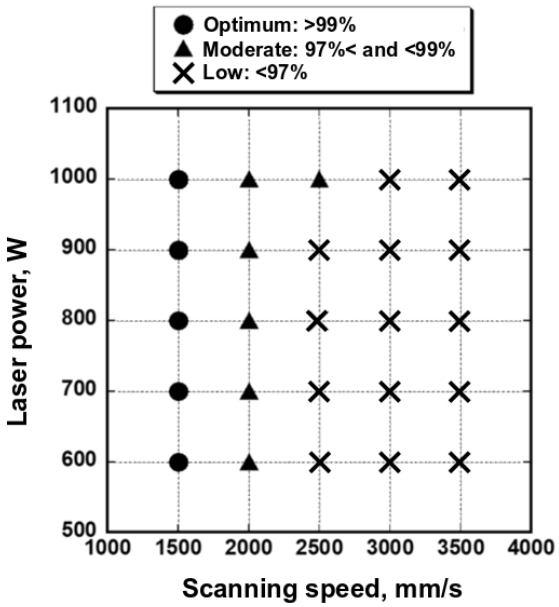

Fig. 14 Process map in terms of the scanning speed and laser power evaluated by the relative density.

[DOI: 10.1299/jamdsm.2023jamdsm0081]

bottom (Fig. 6). However, this agreement is not observed in the region with low scanning velocity 1500 mm/s and low laser power 600-700 W. The input energy density in this region is relatively high > 53.3 J/m^3 (Table 4). Considering the lower scanning velocity, the penetration of the melt pool may become keyhole mode. Christiansen's N-D diagram is based on the conduction mode, in which only heat conduction causes melt pool formation. Nevertheless, when the laser intensity is low scanning velocity, a keyhole is generated in the melt pool to penetrate deeper. The metallurgical microstructure observation of cross-section is required to identify the conduction and keyhole modes.

4.3 Observation of the melt pool behavior

Fig. 15 displays high-speed camera images of the melt pool behavior during laser scanning. Fig. 15(a) presents the image captured with a scanning speed of 4000 mm/s and laser power of 1000 W. The melt pool in the center of the figure did not form a clear teardrop shape. Moreover, although the spatters were emitted in almost all directions, most were backward spatters, and no laser track formation was observed. For Fig. 15(b)-(d), the scanning speed was 1500 mm/s, and the laser power was 1000, 700, and 600 W, respectively. In Fig. 15(b), the bright part in the center of the figure seemed to be the melt pool. The shape of the melt pool seemed stable, although its contour was not clearly defined due to covering it with unmelted powder particles (denudation). However, the melt pool tail swung to the side. The width of the melt pool did not change significantly with laser power: almost 120-150 μm. The tail end of the melt pool was ambiguous, but according to the brightly moving rim of the melt pool tail in the movie, the melt pool length was considered to be less than 1 mm. The gray area surrounding the bright part was the plasma plume, comprising the metal vapor jet and plasma. This plume was emitted upward from the melt surface and remained over the solidified area (i.e., a laser track) for ~0.1 ms. Spatters were ejected backward from the melt pool, while a bright curve following the melt pool was identified as a laser track. The meandering amplitude of the laser track increased with decreasing laser power.

The snapshot of the behavior under the lower power and scanning speed conditions was also added for reference (Fig. 15(e)). Compared to those observed under higher laser power and scanning speed conditions, the melt pool shape and laser track were clearer, indicating that no plume was emitted to hide the melt pool. Moreover, fewer spatters of smaller sizes were observed while the laser track remained straight.

In all observed cases, as detailed in Section 2, it was found that $vt_b < L$, indicating that the melt pool tail did not break up and balling phenomena were absent. Notably, in Fig. 15 (b)-(d), when the scanning speed was set to 1500 mm/s, the observed unstable motion of the melt pool potentially indicates the presence of Rayleigh instability. However, this instability may have been mitigated by the penetration of the melt into the substrate beneath the powder bed, effectively anchoring the melt pool and preventing balling phenomena. The depth of the melt pool, estimated using Christiansen's N-D diagram technique, was sufficient for substrate penetration. It is important to note that the actual melt pool depth exceeded this rough estimate due to the formation of micro keyholes within the melt pool. Therefore, the melt pool depth should be considered in light of micro-keyhole formation and Rosenthal's estimate based solely on heat conduction.

Bidare et al.(Bidare et al., 2018) explained the direction of the spatter ejection using the style of the laser plume inclination, which changed with the scanning speed and laser power. It exhibits a shallow dimple under the laser spot on a melt pool surface, which is the micro-keyhole. When the laser spot travels at a high scanning speed, the direction of laser plume emission changes from the forward to the backward of the micro-keyhole. The plume pushes the liquid metal out of the melt pool, and the liquid metal rides the laser plume to fly backward. Compared to the spatter ejection conditions reported by Bidare et al. (Bidare et al., 2018), the laser power was three- to five-fold, and the scanning speed was 1.5- to 3.5-fold faster in our research. This difference in conditions might have caused the violent movement of the melt pool. The spatter detached from the aft of the melt pool, similar to the behavior observed in the laser surface texturing(Semak and Dahotre, 1998).

This dynamical melt flow may produce defects like lack-of-fusion and keyhole pores. Zhao et al.(Zhao et al., 2017) and Cunningham et al.(Cunningham et al., 2019) reported real-time monitoring of the melt pool profile using high-speed hard X-ray imaging with a synchrotron light source. They reported that quick melting and formation of a narrow, deep keyhole enhanced the spread of the melt out of the melt pool, and a cavity remained at the bottom of the keyhole in the case of high laser power. Therefore, a keyhole pore, increased spatter, and instability of the track

[DOI: 10.1299/jamdsm.2023jamdsm0081]

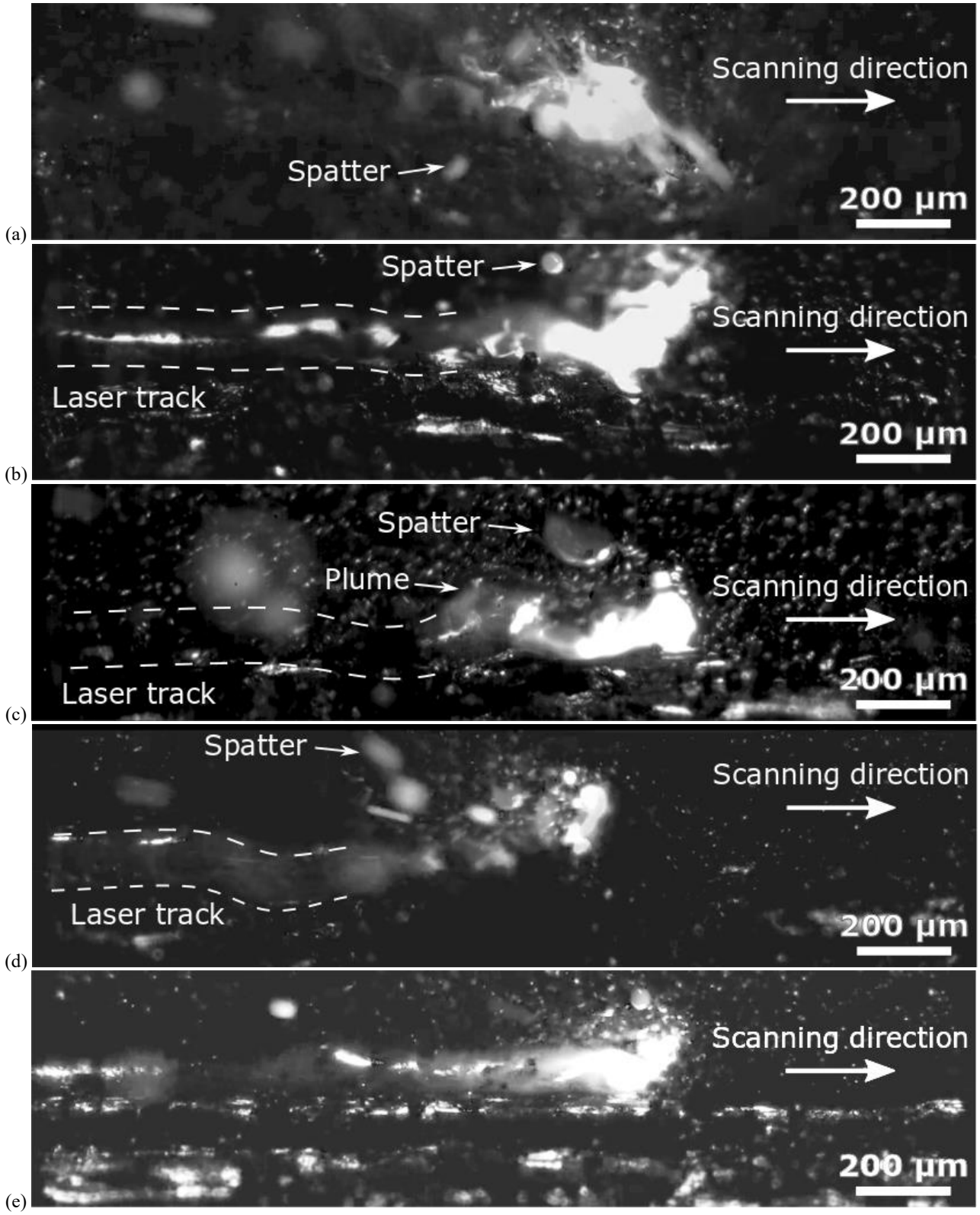

Fig. 15 The behavior of the melt pool under high power and scanning speed conditions captured by high-speed camera imaging at the respective laser powers and scanning speeds of (a) 1000 W and 4000 mm/s, (b) 1000 W and 1500 mm/s, (c) 700 W and 1500 mm/s, (d) 600 W and 1500 mm/s, and (e) 250 W and 600 mm/s (layer thickness, 0.05 mm and hatching pitch, 0.15 mm).

[DOI: 10.1299/jamdsm.2023jamdsm0081]

due to high power and scanning speed caused the fall in the relative densities (Fig. 8).

4.4 Microstructures of the as-built specimens

Fig. 16 presents the macroscopic optical images of the as-built specimen cross-sections. For a laser power of 600 W and a scanning speed of 1500 mm/s, the cross-section of the laser track displayed a cusp shield shape [white dashed outline in Fig. 11 (a). Several lack-of-fusion defects were also observed as well as circular gas pore defects located at the tip of the cusp shape. The laser track cross-section was finger-shaped with a high aspect ratio at 1000 W and 1500 mm/s (Fig. 16(b)). Lack-of-fusion defects were observed along the edge of the finger-shaped fusion zone, while minute spherical gas pore defects were dispersed in the laser track. The gas pore defects were ~10 μm in diameter (Fig. 11(c)). These results suggest that the cross-section shape of the laser track changes from a cusp shield to a finger shape with an increase in the laser power. The cusp shield shape was attributed to the combination of power bed melting and keyhole penetration of the substrate, whereby the former formed the low-aspect-ratio-shield shape, and the latter formed the acute cusp shape. At the lower laser power, the cusp width was narrow, while at the higher laser power, the keyhole penetration widened so that the cusp width became equal to the shield width. Therefore, both Fig. 16(a) and (b) are considered to show laser track formation in the keyhole mode.

At a laser power of 600 W (Fig. 16(a)), the gas pores are relatively large and located at the tips of the cusps and are attributed to the unstableness of the melt pool described in the previous section (Fig. 15(d)). The violent movement at the surface of the melt pool sometimes closes the mouth of the keyhole, leaving a large void at the bottom of the melt pool; the fluctuation in the keyhole depth also leaves a large gas pore(Bidare et al., 2018). At a laser power of 1000 W and a scanning speed of 1500 mm/s, the melt pool surface is stable, and hence, the bubbles of the metal vapor are minute and dispersed (Fig. 15(c)). Lack-of-fusion defects exist along the edge of the fusion zone in both cases despite the difference in laser power. Thus, improving the density of the as-built specimen at high power and scanning speed might be difficult. The occurrence of a keyhole pore increased spatters, and the instability of the track was

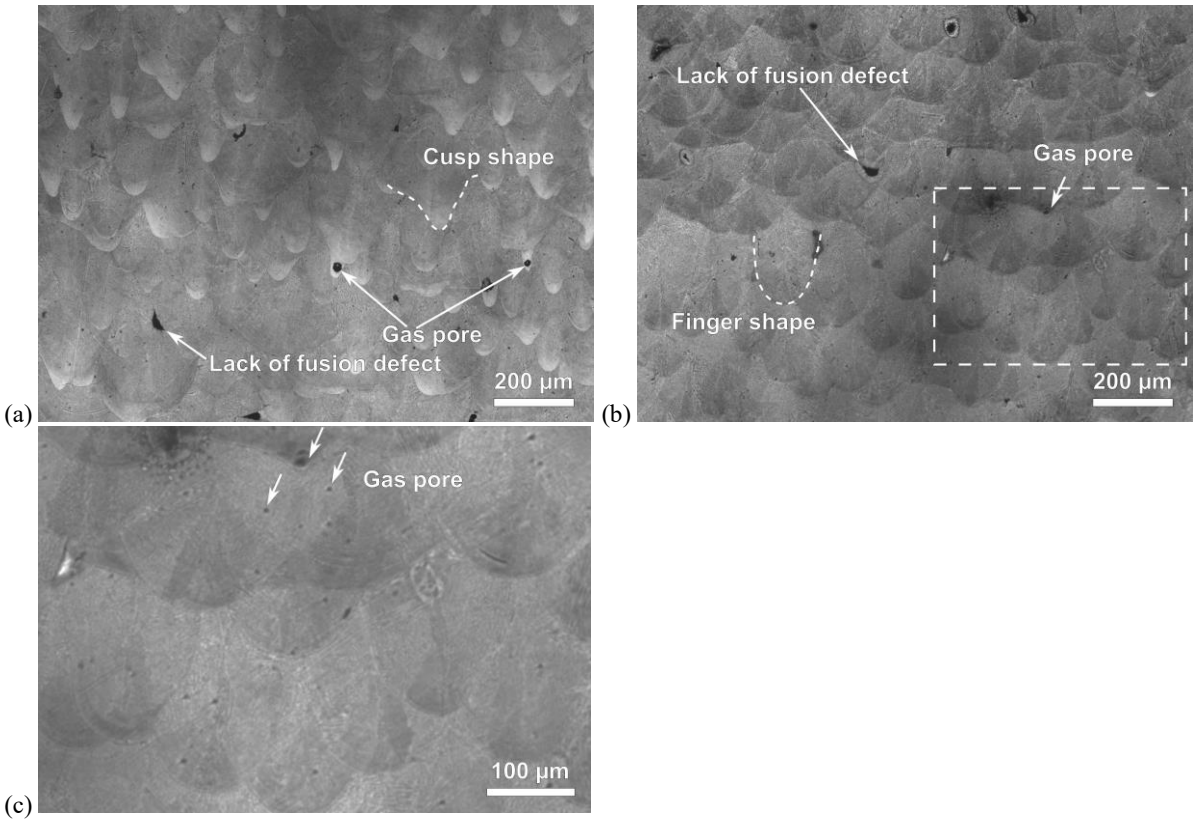

Fig. 16 Cross-section of the as-built specimen with respective laser powers, scanning speeds, and hatching pitch of (a) 600 W, 1500 mm/s, and 0.15 mm and (b) 1000 W, 1500 mm/s, and 0.15 mm. (c) is the area within the dashed line in (b). The white arrows indicate examples of the gas pores resulting from metal vapor bubbles.

[DOI: 10.1299/jamdsm.2023jamdsm0081]

attributed to the high power and scanning speed, as mentioned above.

Fig. 17 illustrates the secondary electron image (SEI) and EDS elemental mapping images of the cross-section of the as-built specimen built at 600 W and 1500 mm/s. The lamellar and columnar structure and the precipitates on the boundary were visible in the SEI, while the apparent dendritic feature of sub-branching could not be observed in the SEI and EDS images. The columnar structure seemed to consist of two phases. In the segregated phase, the precipitates were distributed uniformly. The EDS elemental mapping image for nickel suggested the uniform distribution of nickel, while both niobium and molybdenum presented similar distributions along the columnar arms.

Zhang et al.(Zhang et al., 2015), Chlebus et al.(Chlebus et al., 2015), and Amato et al.(Amato et al., 2012) examined the microstructure of the as-built specimen and observed a laminar and columnar structure composed of the γ-Ni phase matrix. Additionally, they identified the presence of γ"-(Ni3Nb; D022), δ-(Ni3Nb; orthorhombic), and Laves-type (Ni2Nb) phases. In Fig. 17, the lamellar and columnar structure observed is considered the γ phase, while the segregated regions correspond to γ" or δ phases. Based on the findings of Chlebus et al. (Chlebus et al., 2015), it was inferred that the precipitates consisted of Laves-type phases, MC-type carbides, and δ-phase. Chlebus et al. also discussed the dendritic-cellular growth of grains at high cooling rates during the PBF-LB process, attributing the formation of non-equilibrium Laves phases in inter-dendritic spaces, grain boundaries, and layer interfaces to the micro segregation of niobium and molybdenum. The lamellar and columnar structure depicted in Figure 17 represents the γ phase matrix, while the precipitates along the boundaries correspond to γ"-, δ-, and Laves phases, as evidenced by the presence of both niobium and molybdenum elements in the precipitates, as confirmed by the EDS results.

5. Conclusions

For the PBF-LB process of the nickel-based superalloy IN718, the process map was provided in the high laser power range of 600-1000 W and high scanning speed range of 1500-3500 mm/s. The process map was based on the

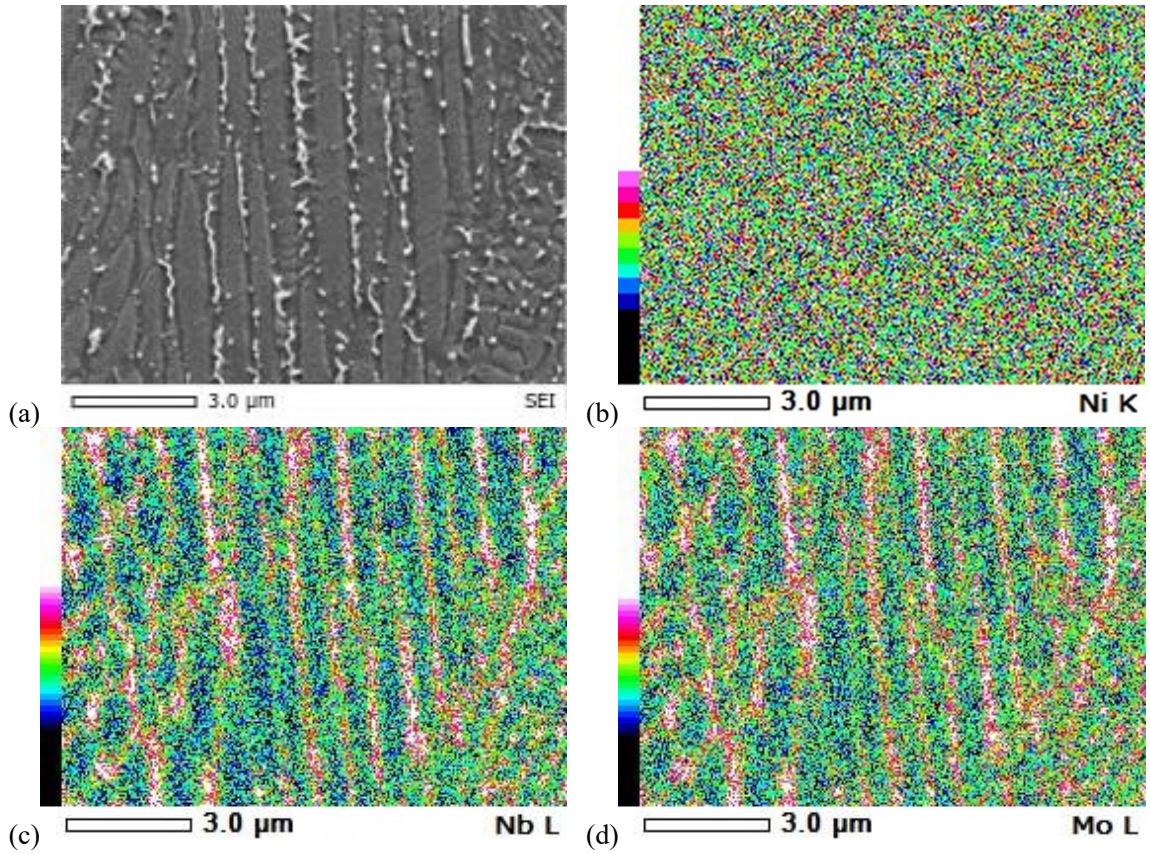

Fig. 17 Microstructure of the as-built specimen built at a laser power of 600 W and scanning speed of 1500 mm/s. (a) The SEI and EDS elemental mapping of (b) nickel, (c) niobium, and (d) molybdenum.

[DOI: 10.1299/jamdsm.2023jamdsm0081]

optical investigation of the specimens' surface morphology and relative density values. The process window where the PBF-LB-built cuboid material had a smooth surface and relative density values >99.5% was the area of the laser power in the range 700-1000 W and a scanning speed of 1500 mm/s.

The process maps based on the surface morphology and the relative density agreed with the process map predicted by the modification of Christiansen's N-D diagram technique with the inclusion of melt pool dimensions on the powder bed bottom.

The behavior of the melt pool under high power and scanning speed conditions was captured using a high-speed camera. The plasma plume was observed to move backward in the laser scan direction, with many large ejected spatters riding on it. The melt pool was unstable while the laser track meandered.

The macroscopic observation of the as-built specimen cross-sections revealed gas pore defects and lack-of-fusion internal defects, which lower the relative density. Notably, the microstructure of the PBF-LB-built IN718 material was similar to the material built under the currently employed low power and scanning speed conditions.

The present research provided the process window for the fully dense built material in the high-power and scanning speed condition range, and those parameter sets, especially high-speed scanning velocity, will lead to a shorter building time compared with the current process window.

Acknowledgments

This paper is based on the results obtained from the project commissioned by the Ministry of Economy, Trade, and Industry and the New Energy and Industrial Technology Development Organization (NEDO). The “Next-generation industrial 3D printer technology project” was performed by the Technology Research Association for Future Additive Manufacturing (TRAFAM).

Reference

Amato, K. N., Gaytan, S. M., Murr, L. E., Martinez, E., Shindo, P. W., Hernandez, J., Collins, S. and Medina, F., Microstructures and mechanical behavior of Inconel 718 fabricated by selective laser melting, Acta Materialia, Vol.60, No.5 (2012), pp.2229-2239, DOI:10.1016/j.actamat.2011.12.032

Araki, M., Kusakawa, S., Nakamura, K., Yonehara, M., Ikeshoji, T.-T. and Kyogoku, H., Parameter Optimization on the Fabrication of Al-10Si-0.4Mg Alloy Using Selective Laser Melting Process, Journal of the Japan Society of Powder and Powder Metallurgy, Vol.65, No.7 (2018), pp.383-388, DOI:10.2497/jjspm.65.383

ASTM A763-15, Standard Practices for Detecting Susceptibility to Intergranular Attack in Ferritic Stainless Steels, ASTM International, DOI:10.1520/A0763-15

Aydinöz, M. E., Brenne, F., Schaper, M., Schaak, C., Tillmann, W., Nellesen, J. and Niendorf, T., On the microstructural and mechanical properties of post-treated additively manufactured Inconel 718 superalloy under quasi-static and cyclic loading, Materials Science and Engineering: A, Vol.669 (2016), pp.246-258, DOI:10.1016/j.msea.2016.05.089

Barros, R., Silva, F. J. G., Gouveia, R. M., Saboori, A., Marchese, G., Biamino, S., Salmi, A. and Atzeni, E., Laser Powder Bed Fusion of Inconel 718: Residual Stress Analysis Before and After Heat Treatment, Metals, Vol.9, No.12, Article number 1290 (2019), pp.1-17, DOI:10.3390/met9121290

Bidare, P., Bitharas, I., Ward, R. M., Attallah, M. M. and Moore, A. J., Fluid and particle dynamics in laser powder bed fusion, Acta Materialia, Vol.142 (2018), pp.107-120, DOI:10.1016/j.actamat.2017.09.051

Bourell, D., Coholich, J., Chalancon, A. and Bhat, A., Evaluation of energy density measures and validation for powder bed fusion of polyamide, CIRP Annals, Vol.66, No.1 (2017), pp.217-220, DOI:10.1016/j.cirp.2017.04.128

Bramfitt, B. L. and Benscoter, A. O., Metallographer’s Guide: Practice and Procedures for Irons and Steels, ASM International (2001), pp.1-354, (online) available from <https://books.google.co.jp/books?id=hoM8VJHTt24C,> (accessed on 11 November, 2023)

Brooks, R. F., Monaghan, B., Barnicoat, A. J., McCabe, A., Mills, K. C. and Quested, P. N., The physical properties of alloys in the liquid and mushy states, International Journal of Thermophysics, Vol.17, No.5 (1996), pp.1151-1161, DOI:10.1007/BF01442002

Cheng, B., Lydon, J., Cooper, K., Cole, V., Northrop, P. and Chou, K., Melt pool sensing and size analysis in laser powder-bed metal additive manufacturing, Journal of Manufacturing Processes, Vol.32 (2018), pp.744-753,

DOI:10.1016/j.jmapro.2018.04.002

Chlebus, E., Gruber, K., Kuźnicka, B., Kurzac, J. and Kurzynowski, T., Effect of heat treatment on the microstructure and mechanical properties of Inconel 718 processed by selective laser melting, Materials Science and Engineering: A, Vol.639 (2015), pp.647-655, DOI:10.1016/j.msea.2015.05.035

Christiansen, N., Davies, V. D. and Gjermundsen, K., Distribution of temperatures in arc welding, British Welding Journal, Vol.2 (1965), pp.54-75.

Cunningham, R., Zhao, C., Parab, N., Kantzos, C., Pauza, J., Fezzaa, K., Sun, T. and Rollett, A. D., Keyhole threshold and morphology in laser melting revealed by ultrahigh-speed x-ray imaging, Science, Vol.363, No.6429 (2019), pp.849-852, DOI:10.1126/science.aav4687

Donachie, M. J. and Donachie, S. J., Superalloys, in Metals Handbook Desk Edition (2nd ed.), edited by Davis, J. R., ASM International (1998), pp.394-414, DOI:10.31399/asm.hb.mhde2.a0003120

Farber, B., Small, K. A., Allen, C., Causton, R. J., Nichols, A., Simbolick, J. and Taheri, M. L., Correlation of mechanical properties to microstructure in Inconel 718 fabricated by Direct Metal Laser Sintering, Materials Science and Engineering: A, Vol.712 (2018), pp.539-547, DOI:10.1016/j.msea.2017.11.125

Fu, S. H., Dong, J. X., Zhang, M. C. and Xie, X. S., Alloy design and development of INCONEL718 type alloy, Materials Science and Engineering: A, Vol.499, No.1-2 (2009), pp.215-220, DOI:10.1016/j.msea.2007.11.115

Gao, Y., Zhang, D., Cao, M., Chen, R., Feng, Z., Poprawe, R., Schleifenbaum, J. H. and Ziegler, S., Effect of δ phase on high temperature mechanical performances of Inconel 718 fabricated with SLM process, Materials Science and Engineering A, Vol.767, Article number 138327 (2019), pp. 1-13, DOI:10.1016/j.msea.2019.138327

Gibson, I., Rosen, D. W. and Stucker, B., Additive manufacturing technologies: Rapid prototyping to direct digital manufacturing, Springer New York (2009), pp.1-459, DOI:10.1007/978-1-4419-1120-9

Grong, Ø., Metallurgical Modelling of Welding (2nd edition), Cambridge: Institute of Materials (1997), pp.1-677, (online) available from <https://books.google.co.jp/books?id=JwNUAAAAMAAJ>, (accessed on 17 November, 2023)

Hayashi, K. and Kakehi, K., Effect of Heat Treatment on Mechanical Properties of Inconel 718, Journal of the Japan Institute of Metals, Vol.74, No.8 (2010), pp.501-507, DOI:10.2320/jinstmet.74.501

Ikeshoji, T. T., Kyogoku, H., Yonehara, M., Araki, M. and Nakamura, K., Numerical Transient Heat Transfer Analysis of Multi Laser Track on Powder Bed of Ni-Based Alloy, Proceedings of the 27th Annual International Solid Freeform Fabrication Symposium (2016), pp.398-405.

ISO/ASTM 52900:2018, Additive manufacturing - General principles - TerminologyISO/ASTM Standards (2018).

Jia, Q. and Gu, D., Selective laser melting additive manufacturing of Inconel 718 superalloy parts: Densification, microstructure and properties, Journal of Alloys and Compounds, Vol.585 (2014), pp.713-721, DOI:10.1016/j.jallcom.2013.09.171

JIS G 0571:2003, Method of oxalic acid etching test for stainless steel. Japanese Standards Association.

Khairallah, S. A., Anderson, A. T., Rubenchik, A. and King, W. E., Laser powder-bed fusion additive manufacturing: Physics of complex melt flow and formation mechanisms of pores, spatter, and denudation zones, Acta Materialia, Vol.108 (2016), pp.36-45, DOI:10.1016/j.actamat.2016.02.014

King, W. E., Anderson, A. T., Ferencz, R. M., Hodge, N. E., Kamath, C. and Khairallah, S. A., Overview of modelling and simulation of metal powder bed fusion process at Lawrence Livermore National Laboratory, Materials Science and Technology, Vol.31, No.8 (2015), pp.957-968, DOI:10.1179/1743284714Y.0000000728

King, W. E., Barth, H. D., Castillo, V. M., Gallegos, G. F., Gibbs, J. W., Hahn, D. E., Kamath, C. and Rubenchik, A. M., Observation of keyhole-mode laser melting in laser powder-bed fusion additive manufacturing, Journal of Materials Processing Technology, Vol.214, No.12 (2014), pp.2915-2925, DOI:10.1016/j.jmatprotec.2014.06.005

Krishnan, M., Atzeni, E., Canali, R., Calignano, F., Manfredi, D., Ambrosio, E. P. and Iuliano, L., On the effect of process parameters on properties of AlSi10Mg parts produced by DMLS, Rapid Prototyping Journal, Vol.20, No.6 (2014), pp.449-458, DOI:10.1108/RPJ-03-2013-0028

Kyogoku, H. and Ikeshoji, T.-T., A review of metal additive manufacturing technologies: Mechanism of defects formation and simulation of melting and solidification phenomena in laser powder bed fusion process, Mechanical Engineering Reviews, Vol.7, No.1, Paper number 19-00182 (2020), pp.1-19, DOI:10.1299/mer.19-00182

Lesyk, D. A., Martinez, S., Mordyuk, B. N., Dzhemelinskyi, V. V., Lamikiz and Prokopenko, G. I., Post-processing of the Inconel 718 alloy parts fabricated by selective laser melting: Effects of mechanical surface treatments on surface

topography, porosity, hardness and residual stress, Surface and Coatings Technology, Vol.381, Article number 125136 (2020), pp.1-16, DOI:10.1016/j.surfcoat.2019.125136

Li, X., Shi, J. J., Wang, C. H., Cao, G. H., Russell, A. M., Zhou, Z. J., Li, C. P. and Chen, G. F., Effect of heat treatment on microstructure evolution of Inconel 718 alloy fabricated by selective laser melting, Journal of Alloys and Compounds, Vol.764 (2018), pp.639-649, DOI:10.1016/j.jallcom.2018.06.112

Lu, Y., Wu, S., Gan, Y., Huang, T., Yang, C., Junjie, L. and Lin, J., Study on the microstructure, mechanical property and residual stress of SLM Inconel-718 alloy manufactured by differing island scanning strategy, Optics and Laser Technology, Vol.75 (2015), pp.197-206, DOI:10.1016/j.optlastec.2015.07.009

Luo, S., Huang, W., Yang, H., Yang, J., Wang, Z. and Zeng, X., Microstructural evolution and corrosion behaviors of Inconel 718 alloy produced by selective laser melting following different heat treatments, Additive Manufacturing, Vol.30, Article number 100875 (2019), pp.1-13, DOI:10.1016/j.addma.2019.100875

Ly, S., Rubenchik, A. M., Khairallah, S. A., Guss, G. and Matthews, M. J., Metal vapor micro-jet controls material redistribution in laser powder bed fusion additive manufacturing, Scientific Reports, Vol.7, No.1, Article number 4085 (2017), pp.1-12, DOI:10.1038/s41598-017-04237-z

Matthews, M. J., Guss, G., Khairallah, S. A., Rubenchik, A. M., Depond, P. J. and King, W. E., Denudation of metal powder layers in laser powder bed fusion processes, Acta Materialia, Vol.114 (2016), pp.33-42, DOI:10.1016/j.actamat.2016.05.017

MatWeb, (a) MetalTek MTEK 718 Cast UNS N07718 Severe Corrosion and Heat Resistant Alloy (online), available from <https://www.matweb.com/search/datasheet.aspx?MatGUID=7d370934d45040d8bf607c28b0feb38d&ckck=1,> (accessed on 17 June, 2020)

MatWeb, (b) Special Metals INCONEL® 718SPFTM Nickel Superalloy, Annealed (online), available from <http://www.matweb.com/search/datasheet.aspx?matguid=b95db0912b2a4b8bb0c39b34d3672c73&ckck=1,> (accessed on 17 June, 2020)

MatWeb, (c) Special Metals INCONEL® Alloy 718, (online) available from <http://www.matweb.com/search/DataSheet.aspx?MatGUID=94950a2d209040a09b89952d45086134,> (accessed on 29 March, 2020)

Moussaoui, K., Rubio, W., Mousseigne, M., Sultan, T. and Rezai, F., Effects of Selective Laser Melting additive manufacturing parameters of Inconel 718 on porosity, microstructure and mechanical properties, Materials Science and Engineering A, Vol.735 (2018), pp.182-190, DOI:10.1016/j.msea.2018.08.037

Ni, M., Chen, C., Wang, X., Wang, P., Li, R., Zhang, X. and Zhou, K., Anisotropic tensile behavior of in situ precipitation strengthened Inconel 718 fabricated by additive manufacturing, Materials Science and Engineering A, Vol.701 (2017), pp.344-351, DOI:10.1016/j.msea.2017.06.098

Nicoletto, G., Smooth and notch fatigue behavior of selectively laser melted Inconel 718 with as-built surfaces, International Journal of Fatigue, Vol.128, Article number 105211 (2019), pp. 1-11, DOI:10.1016/j.ijfatigue.2019.105211

Popovich, V. A., Borisov, E. V., Popovich, A. A., Sufiiarov, V. S., Masaylo, D. V. and Alzina, L., Functionally graded Inconel 718 processed by additive manufacturing: Crystallographic texture, anisotropy of microstructure and mechanical properties, Materials and Design, Vol.114 (2017), pp.441-449, DOI:10.1016/j.matdes.2016.10.075

Rayleigh Sec, R. S. Lord, XVI. On the instability of a cylinder of viscous liquid under capillary force, The London, Edinburgh, and Dublin Philosophical Magazine and Journal of Science, Vol.34, No.207 (1892), pp.145-154.

Rombouts, M., Kruth, J.-P., Froyen, L. and Mercelis, P., Fundamentals of selective laser melting of alloyed steel powders, CIRP Annals, Vol.55, No.1 (2006), pp.187-192.

Rosenthal, D., The Theory of Moving Sources of Heat and Its Application to Metal Treatments, Journal of Fluids Engineering, Vol.68, No.8 (1946), pp.849-865, DOI:10.1115/1.4018624

Sabelkin, V. P., Cobb, G. R., Shelton, T. E., Hartsfield, M. N., Newell, D. J., O'Hara, R. P. and Kemnitz, R. A., Mitigation of anisotropic fatigue in nickel alloy 718 manufactured via selective laser melting, Materials and Design, Vol.1822, Article number 108095 (2019), pp.1-11, DOI:10.1016/j.matdes.2019.108095

Sadowski, M., Ladani, L., Brindley, W. and Romano, J., Optimizing quality of additively manufactured Inconel 718 using powder bed laser melting process, Additive Manufacturing, Vol.11 (2016), pp.60-70, DOI:10.1016/j.addma.2016.03.006

Scime, L. and Beuth, J., Melt pool geometry and morphology variability for the Inconel 718 alloy in a laser powder bed fusion additive manufacturing process, Additive Manufacturing, Vol.29, Article number 100830 (2019), pp.1-9,

[DOI: 10.1299/jamdsm.2023jamdsm0081]

DOI:10.1016/j.addma.2019.100830

Semak, V. V. and Dahotre, N. B., Lasers Surface Texturing. Lasers in surface engineering edited by Dahotre N. B., ASM International (1998), pp.35-68.

Sidambe, A., Derguti, F., Russell, A. and Todd, I., Influence of processing on the properties of IN718 parts produced via Metal Injection Moulding, Powder Injection Moulding International, Vol.4 (2013), pp.65-69.

Tachibana, Y., Araki, M., Ikeshoji, T.-T., Nakamura, K. and Kyogoku, H., Investigation of Fabrication Conditions under High-speed Scanning of INCONEL718 by Selective Laser Melting, The Proceedings of Mechanical Engineering Congress, Japan, Vol.2017, Article number S0460103 (2017), DOI:10.1299/jsmemecj.2017.S0460103

Tachibana, Y., Araki, M., Ikeshoji, T., Nakamura, K. and Kyogoku, H., Microstructure and mechanical properties of Inconel 718 superalloy fabricated by selective laser melting, JSME/ASME 2017 International Conference on Materials and Processing, ICMP2017 (2017), pp.1-5.

Townsend, A., Senin, N., Blunt, L., Leach, R. K. and Taylor, J. S., Surface texture metrology for metal additive manufacturing: a review, Precision Engineering, Vol.46 (2016), pp.34-47, DOI:10.1016/j.precisioneng.2016.06.001

TRAFAM and MAMMS, Bambi Database, IN718_SANYO-Special-Stell(CentrifugalAtomized)_LB(TRAFAM TestBench), (online) available from <https://bambi-element.mamss.co.jp/display?_id=5ddf15fc65b4950018a4c1dc&SIGNED=TRUE&REF=https://bambi.mamss.co.jp/index.html,> (accessed pn 18 June, 2020)

Wang, X. and Chou, K., The effects of stress relieving heat treatment on the microstructure and residual stress of Inconel 718 fabricated by laser metal powder bed fusion additive manufacturing process, Journal of Manufacturing Processes, Vol.48 (2019), pp.154-163, DOI:10.1016/j.jmapro.2019.10.027

Wang, Y., Shi, J., Lu, S. and Wang, Y., Selective Laser Melting of Graphene-Reinforced Inconel 718 Superalloy: Evaluation of Microstructure and Tensile Performance, Journal of Manufacturing Science and Engineering, Vol.139, No.4, Article number 041005 (2016), pp.1-6, DOI:10.1115/1.4034712

Witkin, D. B., Patel, D., Albright, T. V., Bean, G. E. and McLouth, T., Influence of surface conditions and specimen orientation on high cycle fatigue properties of Inconel 718 prepared by laser powder bed fusion, International Journal of Fatigue, Vol.132, Article number 105392 (2020), pp.1-12, DOI:10.1016/j.ijfatigue.2019.105392

Yamashita, Y., Murakami, T., Mihara, R., Okada, M. and Murakami, Y., Defect analysis and fatigue design basis for Ni-based superalloy 718 manufactured by selective laser melting, International Journal of Fatigue, Vol.117 (2018), pp.485-495, DOI:10.1016/j.ijfatigue.2018.08.002

Yang, K. V., Rometsch, P., Jarvis, T., Rao, J., Cao, S., Davies, C. and Wu, X., Porosity formation mechanisms and fatigue response in Al-Si-Mg alloys made by selective laser melting, Materials Science and Engineering A, Vol.712 (2018), pp.166-174, DOI:10.1016/j.msea.2017.11.078

Yap, C. Y., Chua, C. K., Dong, Z. L., Liu, Z. H., Zhang, D. Q., Loh, L. E. and Sing, S. L,. Review of selective laser melting: Materials and applications. Applied Physics Reviews, Vol.2, No.4, Article number 041101 (2015), DOI:10.1063/1.4935926

Yun, Y., Shi, T., Ma, Y., Sun, F., Pan, J. and Yang, Y., Study and Application Status of Additive Manufacturing of Typical Inorganic Non-metallic Materials, Materials Science, Vol.26, No.1 (2019), pp.58-70, DOI:10.5755/j01.ms.26.1.18880

Zhang, D., Niu, W., Cao, X. and Liu, Z., Effect of standard heat treatment on the microstructure and mechanical properties of selective laser melting manufactured Inconel 718 superalloy, Materials Science and Engineering: A, Vol.644 (2015), pp.32-40, DOI:10.1016/j.msea.2015.06.021

Zhao, C., Fezzaa, K., Cunningham, R. W., Wen, H., De Carlo, F., Chen, L., Rollett, A. D. and Sun, T., Real-time monitoring of laser powder bed fusion process using high-speed X-ray imaging and diffraction, Scientific Reports, Vol.7, Article number 3601 (2017), pp.1-11, DOI:10.1038/s41598-017-03761-2

[DOI: 10.1299/jamdsm.2023jamdsm0081]